nature COMMUNICATIONS

ARTICLE

https://doi.org/10.1038/s41467-022-31427-9 OPEN

Boosting electrocatalytic CO_2-to-ethanol production via asymmetric C–C coupling

Pengtang Wang[1,2,4], Hao Yang[3,4], Cheng Tang[1], Yu Wu[3], Yao Zheng[1], Tao Cheng[3], Kenneth Davey[1], Xiaoqing Huang[2✉] & Shi-Zhang Qiao[1✉]

Electroreduction of carbon dioxide (CO_2) into multicarbon products provides possibility of large-scale chemicals production and is therefore of significant research and commercial interest. However, the production efficiency for ethanol (EtOH), a significant chemical feedstock, is impractically low because of limited selectivity, especially under high current operation. Here we report a new silver-modified copper-oxide catalyst ($dCu_2O/Ag_{2.3\%}$) that exhibits a significant Faradaic efficiency of 40.8% and energy efficiency of 22.3% for boosted EtOH production. Importantly, it achieves CO_2-to-ethanol conversion under high current operation with partial current density of 326.4 mA cm^{-2} at −0.87 V vs reversible hydrogen electrode to rank highly significantly amongst reported Cu-based catalysts. Based on in situ spectra studies we show that significantly boosted production results from tailored introduction of Ag to optimize the coordinated number and oxide state of surface Cu sites, in which the $^*CO$ adsorption is steered as both atop and bridge configuration to trigger asymmetric C–C coupling for stablization of EtOH intermediates.

[1] School of Chemical Engineering and Advanced Materials, The University of Adelaide, Adelaide, SA 5005, Australia. [2] State Key Laboratory of Physical Chemistry of Solid Surfaces, College of Chemistry and Chemical Engineering, Xiamen University, Xiamen 361005, China. [3] Institute of Functional Nano & Soft Materials (FUNSOM), Jiangsu Key Laboratory for Carbon-Based Functional Materials & Devices, Joint International Research Laboratory of Carbon-Based Functional Materials and Devices, Soochow University, Suzhou 215123, China. [4] These authors contributed equally: Pengtang Wang, Hao Yang.
✉email: hxq006@xmu.edu.cn; s.qiao@adelaide.edu.au

Electroreduction of carbon dioxide (CO_2) to high-value chemicals and fuels is seen to be practically promising for the utilization of renewable electricity and mitigation of CO_2 emissions, which has emerged as a frontier in energy conversion and carbon neutrality[1–3]. During the CO_2 reduction reaction (CO_2RR), the applied electrical energy is converted to stored chemical energy via reorganizing the molecular bonds in CO_2 and water to generate products with one (C_1), or two or more (C_{2+}) carbon atoms, under the effect of catalysts[4–6]. Most metal catalysts such as gold (Au), silver (Ag), tin (Sn), and lead (Pb) generate a mix of C_1 products[7,8], whilst only Cu-based catalysts transform CO_2 toward C_{2+} products via coupling the adsorbed $^*CO$ intermediates[9–11]. Amongst the various C_{2+} products formed on Cu catalysts, EtOH is important as the liquid fuel because of its wide application and high-energy-density and because it provides the possibility of long-term, large-scale and seasonal energy storage, and convenient transport[3,12]. The production of EtOH with high current density and Faradaic efficiency (FE) via Cu-based catalysts is significant to advancing CO_2RR as a renewable chemical feedstock[2,3,13]. During CO_2RR, EtOH and ethylene (C_2H_4) are both 12-electron reduced products, and share the initial intermediates $^*HCCOH$. Given the more saturated structure of EtOH compared with that for C_2H_4, the next-intermediates for EtOH are more difficult to stabilize on a pure Cu surface compared with C_2H_4. The production of EtOH via C–O bond-reserving of $^*HCCOH$ will therefore have chemical difficulty in competing with C_2H_4 generation. This typically results in the EtOH production in the range of 2–3 times less than that for C_2H_4 on Cu-based catalyst[3,11–14].

To boost EtOH production, research interest has concentrated on optimal re-design of Cu-based catalysts[5,6,15–22]. Strategies including, control of morphology and facet[16,17], vacancy steering[18], dopant and modification engineering[19,20], and defects control[21,22] have been reported. Among these, the modification of Cu with other CO_2-–active metals to form Cu-based bimetallic is reported as practically attractive[15,23–28]. For example, Jaramillo et al. reported Cu–Au bimetallic catalysts with boosted selectivity for CO_2RR to EtOH, and a synergistic catalytic pathway with CO–tandem mechanism was proposed that CO was first generated on Au, desorbed and migrated to near Cu active sites where C–C coupling to EtOH was conducted[24]. Zheng et al. reported a boosted EtOH selectivity in a Cu_3Ag_1 bimetallic catalyst with electron-deficient Cu sites via promoting adsorption of key intermediates[25]. Clark et al. hypothesized that the boosted EtOH selectivity results from Ag-induced strain effects of Cu surfaces that modulate EtOH production and suppresses the hydrogen evolution reaction (HER)[26]. Despite significant progress, the advances of reported bimetallic catalysts for FE of EtOH (FE_{EtOH}) remain limited, especially the production and output efficiency for EtOH is far from the current target for practical application[29–38] (i.e., partial current density > 300 mA cm^{-2} and half-cell cathodic energy efficiencies (EE_{HC}) > 20%). In addition, the key impact of modified components on intrinsic kinetics of reported Cu-based bimetallic catalysts for CO_2RR at high conversion rates is unclear, which significantly hinders understanding of the mechanism and catalyst design[3,14]. Taken together, there is a need therefore for more efficient catalysts and an improved understanding of the mechanism for CO_2RR to practically boost EtOH under commercial current densities.

Here, through modifying Ag onto cubic Cu_2O and activating under CO_2RR, we investigated derived CuAg bimetallics (dCu_2O/Ag) with controlled morphology, phase, and composition for CO_2RR at high current operation. In contrast to the Cu_2O and Au-modified Cu_2O derivatives which favor the conversion of CO_2 to C_2H_4 and CO, respectively, the optimal $dCu_2O/Ag_{2.3\%}$ exhibited an asymmetric C–C coupling to stabilize reaction intermediates for boosted EtOH production under high current density. The as-obtained $dCu_2O/Ag_{2.3\%}$ exhibits FE and EE_{HC} for EtOH of, 40.8% and 22.4%, respectively. We show in a direct comparison with reported catalysts that it has the greatest reported partial EtOH current density with 326.4 mA cm^{-2}. In situ studies confirm that the redispersion of Ag into Cu significantly optimizes the coordinated number and oxide state of Cu. In this way, the $^*CO$ binding strength is altered to form a blended adsorption configuration, that triggers asymmetric C–C coupling for stabilization of EtOH intermediates, and results in boosted EtOH production. This work constructs an efficient catalyst for CO_2RR with high EtOH selectivity at commercially relevant current densities, and provides guidance for designing catalysts with tailored selectivity in multi-electron reactions.

Results

Catalyst preparation and characterization. Pristine Ag-modified Cu_2O nanocubes (Cu_2O/Ag NCs) were prepared by a one-pot seed-medium method in which Cu_2O NCs were achieved via reduction of $Cu(OH)_2$ at room temperature (RT, 25 °C) with ascorbic acid (AA) as a reducing agent, followed by the addition of $AgNO_3$. Because of the appropriate lattice spacing match, the added $AgNO_3$ rapidly nucleates and grows due to the effect of AA to deposit 'small' Ag nanoparticles (Ag NPs) on Cu_2O NCs surface (Fig. 1a). Transmission electron microscopy (TEM) images reveal that the Cu_2O/Ag NCs exhibit heterostructure that Ag NPs sporadically adorn the Cu_2O surface (Fig. 1b and Supplementary Fig. 1a), in comparison to Cu_2O NCs with cubic morphology and a side length of ~45 nm (Supplementary Fig. 2). X-ray photoelectron spectroscopy (XPS) and scanning electron microscopy energy-dispersive X-ray spectroscopy (SEM-EDS) confirm that the Ag NPs in Cu_2O/Ag NCs are metallic, with the content controlled to 2.3% (Fig. 1c and Supplementary Fig. 1b). High-resolution TEM (HRTEM) image highlights the interplanar spacing of the lattice fringes for Cu_2O NCs and Ag NPs regions to be 0.214 nm and 0.236 nm in $Cu_2O/Ag_{2.3\%}$ NCs. This finding is consistent with the Cu_2O (200) plane and Ag (111) plane, respectively (Fig. 1d). Powder X-ray diffraction (XRD) was carried out to confirm the phase of Cu_2O/Ag NCs. It was found that Cu_2O/Ag NCs exhibit the same peak as for Cu_2O NCs which is attributed to the low Ag NPs content (Fig. 1e). In addition, the EDX mapping images for $Cu_2O/Ag_{2.3\%}$ NCs also display an apparent element separation between Ag NPs and Cu_2O NCs, (Fig. 1f). XPS assesses the surface properties of catalysts. The peaks at 951.8 and 931.8 eV for Cu_2O NCs are ascribed to, Cu $2p_{1/2}$ and $2p_{3/2}$, respectively, confirming the presence of Cu(I) in Cu_2O NCs (Fig. 1g)[39]. Following Ag modification, two shoulder peaks for Cu(II) were apparent in the XPS spectra, demonstrating that electrons transfer from Cu_2O to Ag. This finding is validated via the Auger electron spectroscopy (AES) for Cu LMM in which the peaks for $Cu_2O/Ag_{2.3\%}$ NCs downshifts to a lower kinetic energy compared with those for Cu_2O NCs (Supplementary Fig. 3). These findings indicate that an Ag/Cu_2O heterostructure with altered electron structure for Cu_2O was reached with $Cu_2O/Ag_{2.3\%}$ NCs.

Catalyst evolution under CO_2RR. Given the reported evolution of Cu-based catalysts under high current CO_2RR[36], activation and in situ characterization was therefore conducted for $Cu_2O/Ag_{2.3\%}$ NCs to determine the actual state of the catalyst during CO_2RR. A flow cell with gas diffusion electrode (GDE) was especially designed as a reactor for a high current test (Supplementary Fig. 4). As a basis for a detailed comparison, Cu_2O NCs and Au-modified Cu_2O NCs ($Cu_2O/Au_{2.3\%}$ NCs) with similar

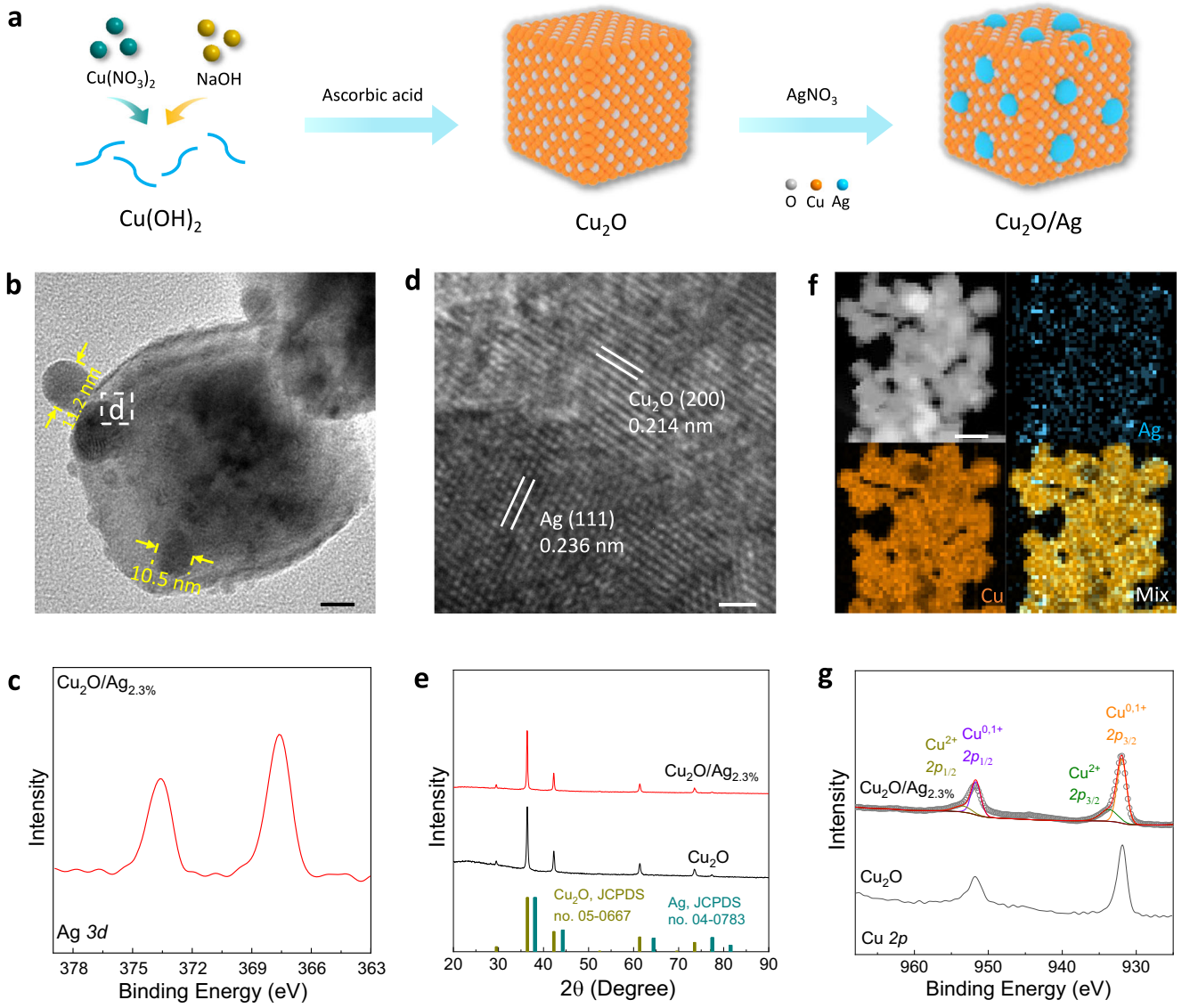

Fig. 1 Structural characterization of Cu_2O/Ag NCs. a Schematic for preparation of Cu_2O/Ag NCs. **b** TEM image, **c** Ag *3d* XPS curve, **d** HRTEM images and **f** EDS elemental mapping images of $Cu_2O/Ag_{2.3\%}$ NCs. **e** XRD patterns and **g** Cu *2p* XPS curves for Cu_2O and $Cu_2O/Ag_{2.3\%}$ NCs. Scale bars, 10 nm in (**b**), 1 nm in (**d**), and 100 nm in (**f**). White-color, orange and azure spheres in the model represent O, Cu, and Ag atoms, respectively.

morphology, composition, and structure to $Cu_2O/Ag_{2.3\%}$ NCs were synthesized and assessed (Supplementary Fig. 5). The catalysts were deposited onto the GDE via spray-coating of the configured ink (details in Supplementary Methods). Activation was controlled by electroreduction of the parent material under CO_2RR at a current density of 200 mA cm^{-2} in 1 M KOH for 30 min. The derived Cu-based catalysts obtained following activation supported on the GDE, denoted as dCu_2O, dCu_2O/Ag, and dCu_2O/Au, were subjected to additional characterization.

High-angle annular dark-field scanning TEM (HAADF STEM) and SEM images confirm that following activation the original cubic morphology and surface deposited NPs are visually less pronounced, and that instead, ragged surface and hollow structures formed in $dCu_2O/Ag_{2.3\%}$ and $dCu_2O/Au_{2.3\%}$ (Fig. 2a and Supplementary Figs. 6 and 7a). Concomitantly, the original surface phase separation between deposited metal and Cu is lost following activation as is confirmed in EDS mapping images (Fig. 2a, Supplementary Fig. 7b). The lattice space for $dCu_2O/Ag_{2.3\%}$ was altered to 0.210 nm following activation, a value near to the Cu (111) facet (Fig. 2b). Ex situ XRD patterns reveal that the diffraction peaks for Cu_2O for all catalysts are decreased significantly whilst the diffraction peaks for Cu became dominant. This finding demonstrates that all catalysts are transformed to mainly metallic Cu following activation (Supplementary Fig. 8). Compared with dCu_2O, the XRD peaks of Cu (111) for $dCu_2O/Ag_{2.3\%}$ and $dCu_2O/Au_{2.3\%}$ exhibit a meaningful, slight shift to a higher degree to underscore that the original Cu_2O/metal heterostructures are evolved into the bimetallic alloy following activation (Fig. 2c).

To gain insight into the changed valence states and coordination environment of Cu following activation, *operando* X-ray absorption spectra (XAS) of Cu K-edge was recorded under activation conditions. The X-ray absorption near-edge structure (XANES) spectra show that the edge features for dCu_2O, $dCu_2O/Ag_{2.3\%}$, and $dCu_2O/Au_{2.3\%}$ are closed to those for the reference commercial Cu-foil. This finding confirms that the valence state for Cu for these catalysts decrease following activation to lie between 0 and +1, in following ordered sequence, $dCu_2O < dCu_2O/Ag_{2.3\%} < dCu_2O/Au_{2.3\%}$ (Fig. 2d). The wavelet transform analysis confirms that the Cu–Cu region in all activated catalysts are located at ~6.7 $Å^{-1}$,

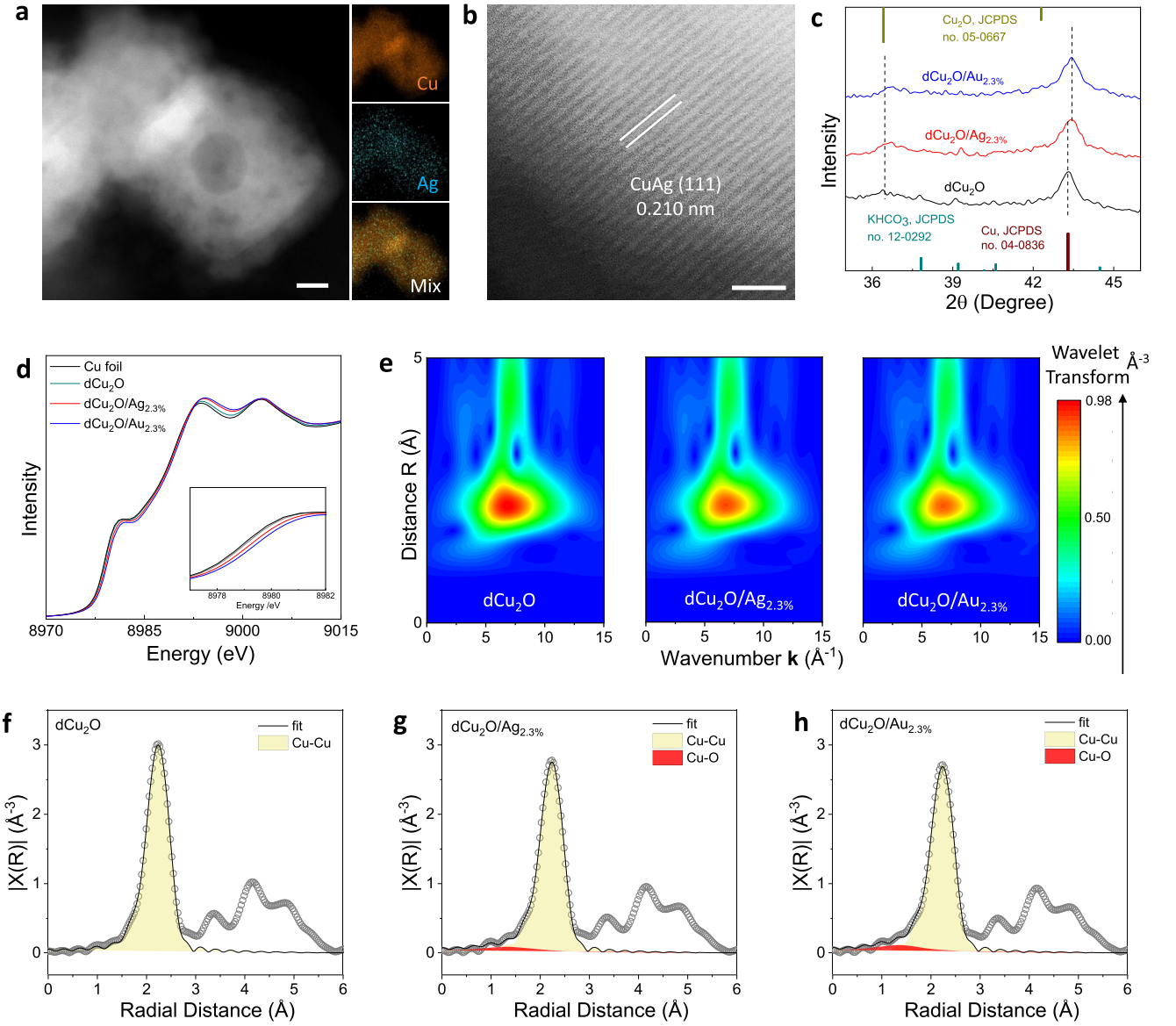

Fig. 2 Phase and coordination environment for dCu_2O/Ag catalysts. a HAADF-STEM image with EDS elemental mappings and **b** high resolution STEM image of $dCu_2O/Ag_{2.3\%}$. **c** Enlarged XRD patterns for dCu_2O, $dCu_2O/Ag_{2.3\%}$ and $dCu_2O/Au_{2.3\%}$. **d** In situ XANES spectra and **e** Wavelet transform images of EXAFS data with optimized Morlet parameter (i.e., $\kappa = 5$, $\sigma = 1$) at Cu K-edge for commercial Cu-foil, dCu_2O, $dCu_2O/Ag_{2.3\%}$ and $dCu_2O/Au_{2.3\%}$. Fourier transform curves of in situ EXAFS data and corresponding fitted results (first coordination shell) for **f** dCu_2O, **g** $dCu_2O/Ag_{2.3\%}$ and **h** $dCu_2O/Au_{2.3\%}$. Scale bars, 10 nm in (**a**) and 1 nm in (**b**).

suggesting that the alloyed CuAg and CuAu do not result in significant change in Cu–Cu bond length compared with the oxide-derived Cu (Fig. 2e). The corresponding Fourier transform curves (from extended X-ray absorption fine structure (EXAFS) spectra) and fitted results of the first coordination shell for these activated catalysts show that the Cu–Cu coordination located at ~2.23 Å is the dominant structure in each sample, whilst there remains another Cu–O coordination peak at 1.35 Å for $dCu_2O/Ag_{2.3\%}$ and $dCu_2O/Au_{2.3\%}$. This finding confirms that a significantly small fraction of Cu(I) remained for $dCu_2O/Ag_{2.3\%}$ and $dCu_2O/Au_{2.3\%}$ following activation (Fig. 2f–g and Supplementary Table 1). The coordination number for Cu−Cu in these catalysts was determined to equal, respectively, 11.4, 10.5, and 10.2 for dCu_2O, $dCu_2O/Ag_{2.3\%}$, and $dCu_2O/Au_{2.3\%}$ (Supplementary Fig. 9). Except for variation in Cu, the XPS for Ag *3d* for $dCu_2O/Ag_{2.3\%}$ shows that the binding energy for Ag $3d_{5/2}$ shifts to a high level following activation. This evidences that the activation of alloying Ag with Cu induces electron transfer (Supplementary Fig. 10). Based on the foregoing, it is concluded that under electroreduction with highly significant structural rearrangement, the pristine metal-modified Cu_2O NCs evolves to Cu-based bimetallics in a regulated valence and coordination environment.

CO_2RR performance. CO_2RR performance for the activated catalysts was directly evaluated via electrolyzing at specified currents (Supplementary Fig. 11). Figure 3a shows the linear sweep voltammetry curves for dCu_2O, $dCu_2O/Ag_{2.3\%}$ and $dCu_2O/Au_{2.3\%}$. It is seen in the figure that the current density for CO_2RR of $dCu_2O/Ag_{2.3\%}$ and $dCu_2O/Au_{2.3\%}$ are significantly increased, directly evidencing that modification boosted activity for CO_2RR. The FEs were computed for liquid and gaseous product in the applied current range 200–800 mA in 1 M KOH by nuclear magnetic resonance (NMR, Supplementary Fig. 12) and gas

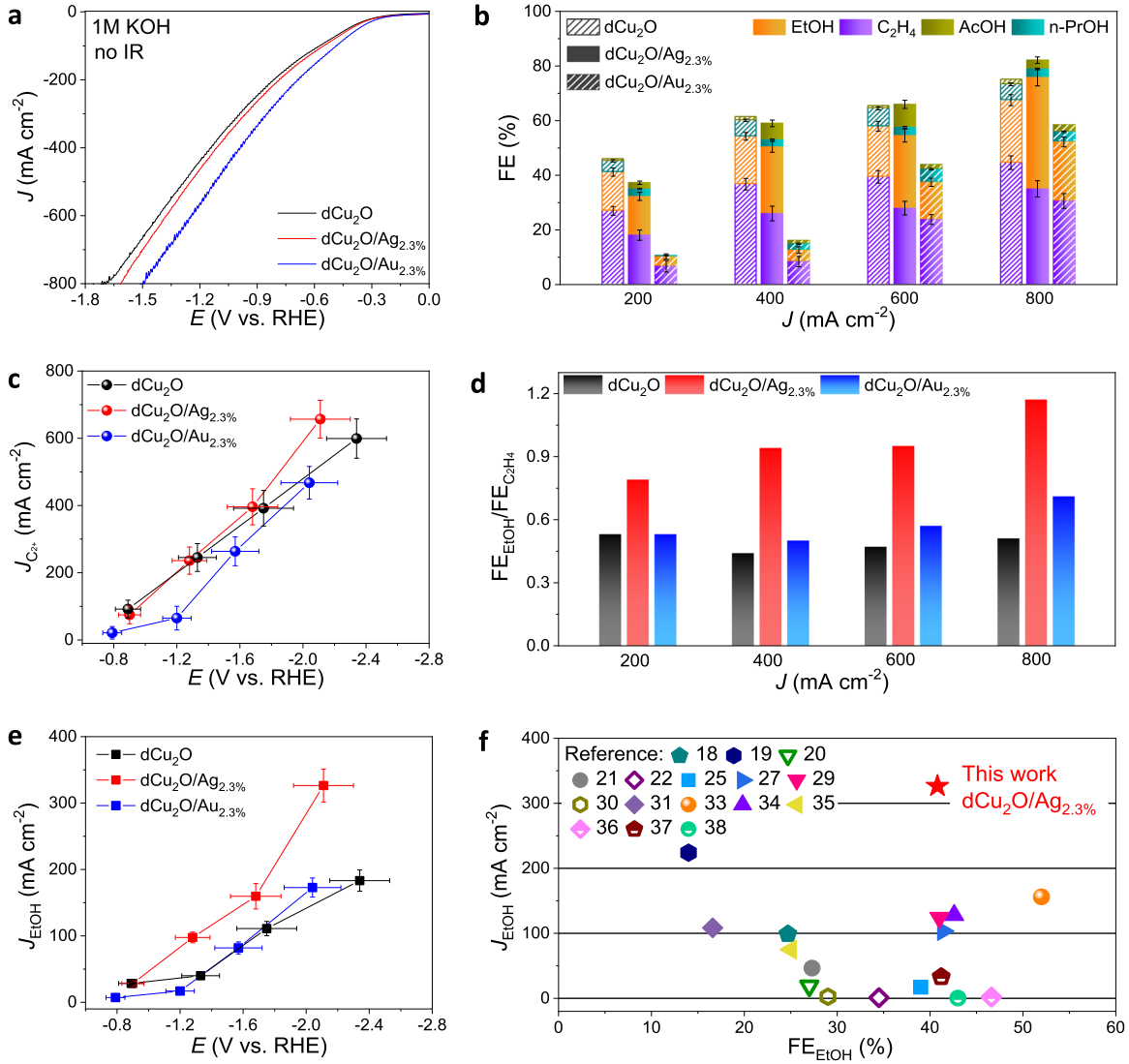

Fig. 3 CO_2RR performance for dCu_2O, $dCu_2O/Au_{2.3\%}$ and $dCu_2O/Ag_{2.3\%}$. **a** Linear sweep voltammetry curves toward CO_2RR for dCu_2O, $dCu_2O/Au_{2.3\%}$ and $dCu_2O/Ag_{2.3\%}$. **b** FE value of C_{2+} products for dCu_2O, $dCu_2O/Au_{2.3\%}$ and $dCu_2O/Ag_{2.3\%}$ under selected current density. **c** Partial C_{2+} current density and **e** C_{2+} formation *vs* potential referred to reversible hydrogen electrode (RHE) on dCu_2O, $dCu_2O/Au_{2.3\%}$, and $dCu_2O/Ag_{2.3\%}$. **d** Ratio of FE_{EtOH} to FE_{C2H4} on dCu_2O, $dCu_2O/Au_{2.3\%}$, and $dCu_2O/Ag_{2.3\%}$ under selected current density. **f** EtOH partial current density *vs* FE_{EtOH} for reported Cu-based catalysts. Error bars correspond to the standard deviation of three independent measurements.

chromatography (GC) (Supplementary Fig. 13) respectively. Figure 3b presents the FEs of C_{2+} products (FEs_{C2+}) for these catalysts under different current. C_2H_4 and EtOH are the major C_{2+} products, plus minor acetate and n–propanol. With the applied current increased, all catalysts exhibited increased FEs_{C2+} and a decreased FEs of CO (FEs_{CO}). Compared with the one–up FE_{C2+} for dCu_2O from 200 to 400 mA, $dCu_2O/Ag_{2.3\%}$ exhibits greater FE_{C2+} at significant current > 600 mA. Importantly, the total FE_{C2+} for $dCu_2O/Ag_{2.3\%}$ is up to 82.1% at a current density 800 mA cm^{-2}, to exhibit the greatest partial C_{2+} current density of 656.8 mA cm^{-2} and formation rate of 2042.2 μmol h^{-1} cm^{-2} at −2.11 V with reference to the reversible hydrogen electrode (V_{RHE}, no *iR* correction, Fig. 3c and Supplementary Fig. 14a). In contrast, the FE_{C2+} for $dCu_2O/Au_{2.3\%}$ is significantly less than that for $dCu_2O/Ag_{2.3\%}$ at all currents, confirming that the Au modification resulted in directly boosting only targeted CO generation, but not C–C coupling.

We analyzed the ratio of FE_{EtOH}/FE_{C2H4} in C_{2+} products at high current density on these catalysts. It is interesting that $dCu_2O/Ag_{2.3\%}$ reaches the FE_{EtOH}/FE_{C2H4} ratio 1.17 at an applied current 800 mA, which is significantly greater than that for dCu_2O (0.51) and $dCu_2O/Au_{2.3\%}$ of 0.71. This finding confirms that the Ag modification significantly inhibits C–O bond-breaking and stabilizes intermediates for EtOH vs C_2H_4 (Fig. 3d). Relying on the boosted FE_{EtOH} of 40.8 % at a high current density (800 mA cm^{-2}), the $dCu_2O/Ag_{2.3\%}$ exhibits the greatest partial EtOH current density of 326.4 mA cm^{-2} at −2.11 V_{RHE} (no *iR* correction, −0.89 V_{RHE} with 85% *iR* correction, Supplementary Figs. 15 and 16). Importantly, this is 1.78 and 1.89 times greater than that for dCu_2O and $dCu_2O/Au_{2.3\%}$, respectively (Fig. 3e). The EtOH formation for $dCu_2O/Ag_{2.3\%}$ could reach 1014.9 μmol h^{-1} cm^{-2} with current densities of 800 mA cm^{-2} at −2.11 V_{RHE} (without *iR* correction) (Supplementary Fig. 14b). Such highly significant performances for EtOH production on $dCu_2O/Ag_{2.3\%}$ were compared directly with reported catalysts (Fig. 3f, Supplementary Table 2). It is apparent that the $dCu_2O/Ag_{2.3\%}$ exhibits the greatest reported partial EtOH current density amongst these, and represents the 'best' production for electroreduction of CO_2 to EtOH. In addition, the EE_{HC} for EtOH on $dCu_2O/Ag_{2.3\%}$ reaches 22.4% following *iR* correction under similar conditions, a

value greater than that for most catalysts (Supplementary Fig. 16d). In addition, the electrochemically active surface area (ECSA) for $dCu_2O/Ag_{2.3\%}$ was computed via different methods and compared, together with mass normalized current density for EtOH (J_{ECSA}(EtOH) and J_{mass}(EtOH)) with independently reported studies (Supplementary Figs. 17 and 18 and Supplementary Table 3). The $dCu_2O/Ag_{2.3\%}$ exhibited superior J_{ECSA}(EtOH) and J_{mass}(EtOH) compared with reported catalysts, confirming that the improved EtOH current density for $dCu_2O/Ag_{2.3\%}$ is because of the intrinsic Ag-modified oxide-derived Cu sites and not the changed ECSA and mass loading of the catalyst itself.

Based on these findings therefore of highly significant FE_{EtOH} with high current density from $dCu_2O/Ag_{2.3\%}$ on CO_2RR, a series of Cu_2O/Ag NCs with different amounts of modified Ag were assessed for CO_2RR performance (Supplementary Figs. 19 and 20). Characterizations underscore that all pristine Cu_2O/Ag NCs with different compositions exhibit similar structures, whereas the density of deposited NPs and oxidation state on the surface of Cu_2O NCs increased with the degree of modification (Supplementary Fig. 21). From the comparison of the potential for CO_2RR of different catalysts at a high current density of 800 mA cm^{-2} (Fig. 4a), it can be seen that the demand potential decreases with increased Ag. This finding confirms the positive impact of Ag modification on CO_2RR. The degree of introduced Ag-dependent FEs of products from these catalysts was assessed under the same current density. As is shown in Fig. 4b, c, increasing Ag in dCu_2O/Ag leads to a volcano-shape for FE_{EtOH} that corresponds with a reverse-volcano on FE_{CO}, and contrasts with the monotonously decreased FE for C_2H_4. This correlation between the amount of modified Ag and FEs for CO and EtOH was observed also with other applied currents (Supplementary Fig. 22). Common to Cu-based catalysts, the coverage of CO on Cu surface is conducive to C–C coupling to impact EtOH and C_2H_4 generation concurrently[24]. However, here for the dCu_2O/Ag, only the FE for EtOH exhibits the dependent correlation with CO. These results indicate that the boosted EtOH is not only dependent on variable CO coverage on dCu_2O/Ag, but also related to other unknown factors.

The stability of $dCu_2O/Ag_{2.3\%}$ was evaluated via long-term chronopotentiometry testing. It was found that there is no apparent decay of activity with 6 h continuous operation, in which the selectivity of EtOH decreased ~6% following CO_2RR (Supplementary Fig. 23). TEM image and XRD pattern of spent $dCu_2O/Ag_{2.3\%}$ showed that morphology and structure are maintained following the stability test (Supplementary Fig. 24). Given the superior EtOH production on $dCu_2O/Ag_{2.3\%}$, it was consequently assessed in a commercially relevant membrane electrode assembly (MEA) (Supplementary Fig. 25). It was found that there is a good, linear relationship between applied current and voltage in the MEA (Fig. 4e). The FEs for all products tested in flow cell electrolyzer were well-reproduced in MEA (Supplementary Fig. 26 and Fig. 4d), identifying that high current and high EtOH selectivity can be maintained under commercially relevant conditions (Fig. 4e). Importantly, the durability of CO_2RR in the catholyte–free MEA significantly outperformed the flow cell electrolyzer, which exhibited a decrease of FE_{EtOH} (~3%) in 12 h operation under a full–cell voltage of −4.72 V with a total current density 800 mA cm^{-2}, evidencing the good stability of $dCu_2O/Ag_{2.3\%}$ for CO_2RR (Fig. 4f).

Mechanistic studies. The CO reduction reaction (CORR) on dCu_2O/Ag was assessed to identify whether boosted C–C coupling and EtOH generation followed a classic CO–tandem mechanism (Supplementary Fig. 27). To permit a direct comparison, the CORR behavior of dCu_2O and $dCu_2O/Au_{2.3\%}$ were evaluated and the catalysts were activated by a similar process with CO_2RR. It was expected that if the CO–tandem mechanism dominated, the CORR performance for the catalysts would be similar[28]. However, as is shown in Supplementary Fig. 28, the $dCu_2O/Ag_{2.3\%}$ exhibits significant suppression of H_2 and promoted C–C coupling for C_{2+} products under CORR. This is in significant contrast to $dCu_2O/Au_{2.3\%}$ and dCu_2O results. The partial current density of C_{2+} products for $dCu_2O/Ag_{2.3\%}$ reaches 696.0 mA cm^{-2} at −1.56 V_{RHE} for CORR, and is significantly greater than those for $dCu_2O/Au_{2.3\%}$ (~154.0 mA cm^{-2}) and dCu_2O (~188.0 mA cm^{-2}). Similarly, the ratio FE_{EtOH}/FE_{C2H4} for $dCu_2O/Ag_{2.3\%}$ is also greater than that for $dCu_2O/Au_{2.3\%}$ and dCu_2O under CORR. Significantly, these findings from $dCu_2O/Ag_{2.3\%}$ contrast with those for reported Cu–Ag catalyst with CO–tandem mechanism. This is interpreted that Ag modification results in intrinsic property changes in Cu active sites to: (1) suppress HER, (2) improve C–C coupling activity, and; (3) boost EtOH selectivity. In addition, the modification induced compressive strain, and morphology effects (crystal facets) for boosted EtOH production can be also excluded in our circumstances, because the exposed facets, surface structure and Cu–Cu bond length of both $dCu_2O/Au_{2.3\%}$ and $dCu_2O/Ag_{2.3\%}$ catalysts are similar. Therefore, other potential mechanisms on $dCu_2O/Ag_{2.3\%}$ need to be assessed for boosted CO_2RR performance.

Reaction pathways for C_2H_4 and EtOH production are similar on Cu surfaces, as they initiate with two adsorbed–CO dimerization followed by several steps of protonation and dehydration to generate a shared intermediate, $^*HCCOH$[3,14]. The selectivity between C_2H_4 and EtOH, is significantly dependent on the relative stabilities of the next-intermediates for EtOH and C_2H_4 pathways branched from $^*HCCOH$ on Cu sites[3,14,40]. Cu with a relatively low coordinated surface and optimal oxide state is favorable for EtOH generation over C_2H_4 because the reaction intermediates for EtOH are more saturated compared with those for C_2H_4[41], and the existing oxidation is feasible to binding of key oxygen-bound intermediates for EtOH generation[33,42]. Combined with this and previous experiment results, it is hypothesized that Ag-induced the moderate coordinated surface and optimal oxidation of Cu in $dCu_2O/Ag_{2.3\%}$ are responsible for boosted EtOH selectivity. Therefore, the CO_2RR intermediates chemisorbed on dCu_2O, $dCu_2O/Ag_{2.3\%}$, and $dCu_2O/Au_{2.3\%}$ at different potentials were assessed via in situ attenuated total reflectance infrared absorption spectroscopy (ATR–IRAS) to determine the mechanism for boosted EtOH.

As is shown in Fig. 5a, b and Supplementary Fig. 29, with the cathode potential at −0.3 V_{RHE}, the ATR–IRAS spectra for these catalysts exhibit several new peaks. These are assigned to corresponding intermediates based on independently reported studies (Supplementary Table 4). In particular, there appear two peaks at 2044 and 1923 cm^{-1} for $dCu_2O/Ag_{2.3\%}$, which are associated with the atop–adsorbed $^*CO$ ($^*CO_{atop}$) and bridge–adsorbed $^*CO$ ($^*CO_{bridge}$) on Cu surface, respectively[43–45]. In comparison, dCu_2O and $dCu_2O/Au_{2.3\%}$ mainly show the $^*CO_{atop}$ peak with little evidence of $^*CO_{bridge}$ binding in the same potential region. The different $^*CO$ binding configurations on these catalysts can also be observed from CO temperature-programmed desorption (CO–TPD) (Supplementary Fig. 30b). Mathematical integration and statistical analyses confirm the ratio $^*CO_{bridge}/^*CO_{atop}$ for $dCu_2O/Ag_{2.3\%}$ is significantly greater than that for dCu_2O or $dCu_2O/Au_{2.3\%}$ over the potential range (Supplementary Fig. 31 and Fig. 5c). These findings evidence that

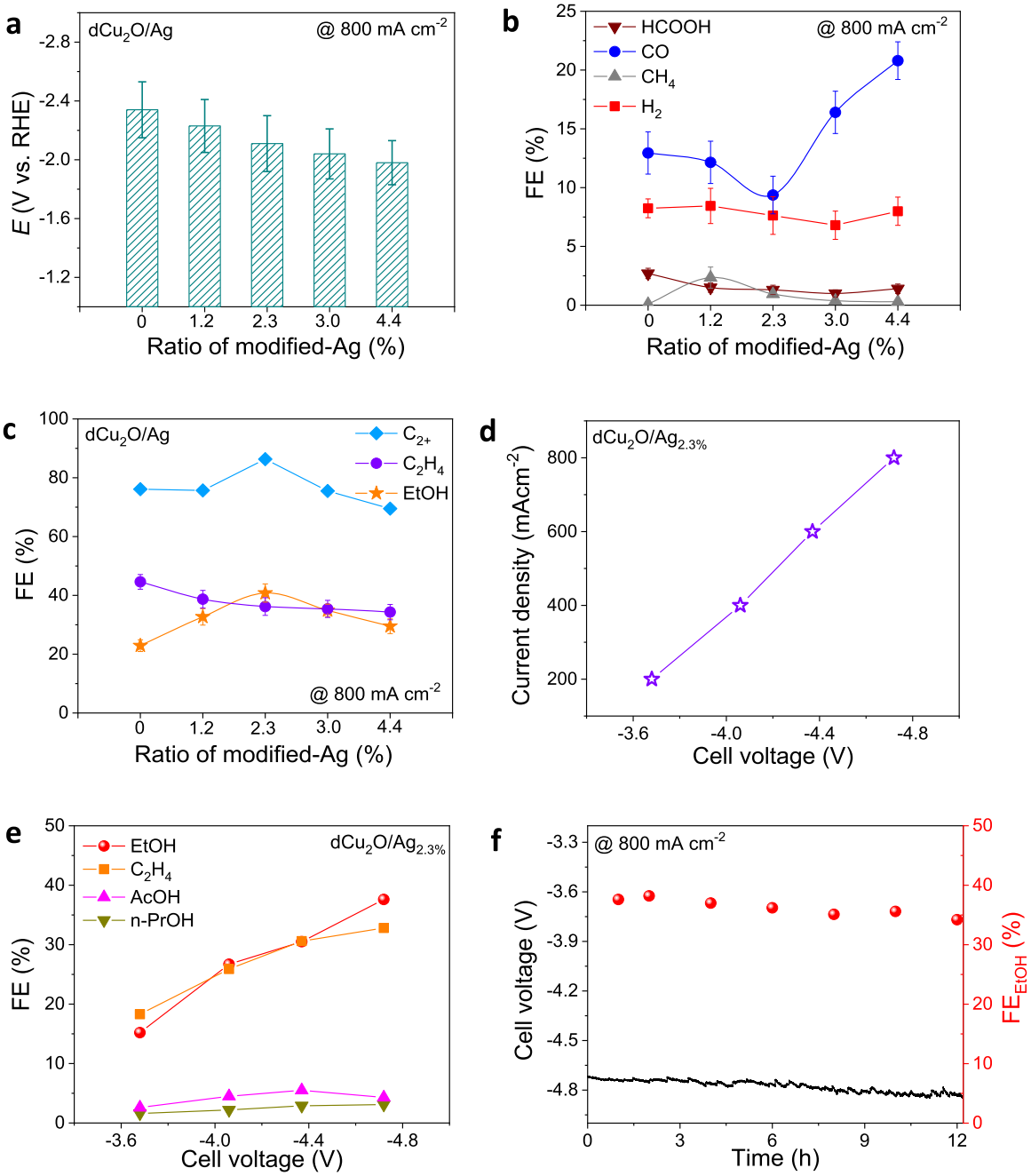

Fig. 4 CO_2RR performance for dCu_2O/Ag with modified Ag. Comparison of **a** applied potentials, **b** FEs for C_1 and H_2 product, **c** FEs for C_2H_4 and EtOH and total C_{2+} product on dCu_2O/Ag with modified Ag at current density 800 mA cm^{-2}. **d** Total current density and **e** FEs for C_{2+} product for CO_2RR on $dCu_2O/Ag_{2.3\%}$ at selected cell voltage under MEA measurement. **f** Stability test for $dCu_2O/Ag_{2.3\%}$ at the current density 800 mA cm^{-2} in MEA. Error bars correspond to the standard deviation of three independent measurements.

compared with dCu_2O and $dCu_2O/Au_{2.3\%}$, the moderate coordination numbers and optimal oxidation for Cu surface in $dCu_2O/Ag_{2.3\%}$ result in tailored *CO configuration. Given the different electron back-donating and proton-combining ability of adsorbed *CO on atop and bridge Cu sites, the energy barrier for following *CO protonation is altered. Previous studies demonstrate that $^*CO_{bridge}$ protonation is more energetically favorable than that of $^*CO_{atop}$ on Cu surface[46]. Therefore, the C–C coupling on $dCu_2O/Ag_{2.3\%}$ could be triggered under asymmetry between *CO and *CHO (or *COH) following the $^*CO_{bridge}$ protonation step. Notably, adsorbed *CHO intermediate was observed on $dCu_2O/Ag_{2.3\%}$ from ATR-FTIR spectra, and increased with the applied potential (Fig. 5b), strongly evidencing this process. This asymmetric C−C coupling has a lower energy barrier than that for *CO dimerization as evidenced by the reported theory studies[19], which contributes to increased C_{2+} production.

Additional peaks from ATR–IRAS spectra at ~1567 and ~1182 cm^{-1} and ~1336 and ~1117 cm^{-1} were analyzed. These peaks, indexed to the absorbed $^*OCCOH$ and $^*OC_2H_5$ on these catalysts, exhibit a ratio value for $^*OC_2H_5/^*OCCOH$ on $dCu_2O/Ag_{2.3\%}$ that is significantly greater compared with that for dCu_2O and $dCu_2O/Au_{2.3\%}$. This finding evidences that the key $^*OC_2H_5$ intermediates for EtOH production are more stable on

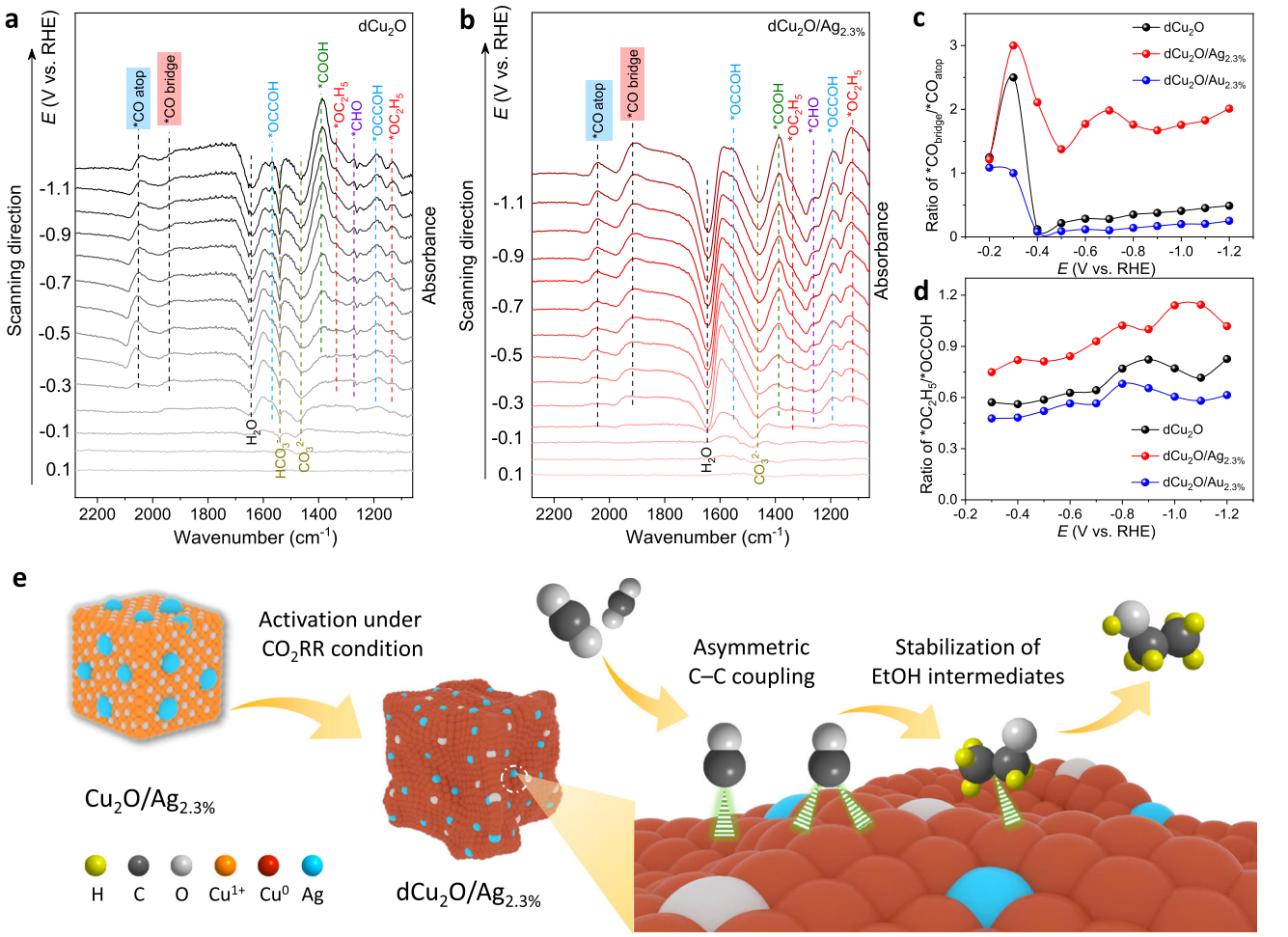

Fig. 5 In situ ATR-IRAS measurement and mechanism for $dCu_2O/Ag_{2.3\%}$. In situ ATR-IRAS obtained during chronopotentiometry in a potential window 0.2 to −1.2 V_{RHE} for **a** dCu_2O, and **b** $dCu_2O/Ag_{2.3\%}$ under CO_2RR. (A reference spectrum obtained at 0.3 V_{RHE} in 1 M KOH is subtracted). Potential dependence of ratio of **c** $^*CO_{bridge}/^*CO_{atop}$ and **d** $^*OC_2H_5/^*OCCOH$ obtained for dCu_2O, $dCu_2O/Ag_{2.3\%}$ and $dCu_2O/Au_{2.3\%}$. **e** Schematic for boosted EtOH generation over $dCu_2O/Ag_{2.3\%}$. Yellow-color, gray, white, orange, red, and azure spheres in the model represent H, C, O, Cu^{1+}, Cu^0, and Ag atoms, respectively.

$dCu_2O/Ag_{2.3\%}$ (Fig. 5d)[42,43]. This is attributed to the asymmetric C−C coupling induced unbalanced coordination environment, which disrupts the coordination sites for C_2H_4 intermediates, and thereby, stabilizes the EtOH intermediates. This is in agreement with report that diversity of $^*CO$ binding site enhances C_{2+} liquid product formation[27]. Therefore we hypothesize that triggered asymmetric C−C coupling on $dCu_2O/Ag_{2.3\%}$ boosts C_{2+} production and favors EtOH pathway via stabilizing pivotal intermediates.

In addition, the peak for the absorbed bicarbonate at 1547 cm^{-1} on $dCu_2O/Ag_{2.3\%}$ is missing compared with dCu_2O and $dCu_2O/Au_{2.3\%}$, confirming that the value of the local pH on the electrode of $dCu_2O/Ag_{2.3\%}$ is greater than that for dCu_2O and $dCu_2O/Au_{2.3\%}$ during CO_2RR[47]. The high pH at the surface of electrode is thought to favor C–C coupling by lowering the energy barrier of CO_2 activation and suppressing H_2 evolution, and contributes to the boosted activity for CO_2RR. Moreover, the CO–TPD and CO_2–TPD for $dCu_2O/Ag_{2.3\%}$ also exhibit a higher temperature for CO_2 and CO desorption than those for dCu_2O and $dCu_2O/Au_{2.3}$, indicating $dCu_2O/Ag_{2.3\%}$ has stronger bonding strength of CO_2 and CO for efficient CO_2RR at large current (Supplementary Fig. 30).

Accordingly, based on the ATR–IRAS spectra analysis, the mechanism for boosted EtOH on $dCu_2O/Ag_{2.3\%}$ can be soundly proposed (Fig. 5e). At first, the coordinated pure-Cu surface is replaced with neighboring Ag atoms with modification by Ag in Cu_2O and reduces these to CuAg alloy under CO_2RR. Then, the Ag-induced moderate coordination numbers and optimal oxidation of Cu surface regulate binding strength of $^*CO$, to configure mixed $^*CO_{bridge}$ and $^*CO_{atop}$ adsorption that triggers asymmetric C–C coupling after $^*CO_{bridge}$ protonation. Because of the relatively low oxygen affinity and unsaturated nature of the C_2H_4 intermediates compared with EtOH, the asymmetric C–C coupling provides an unbalanced coordination environment that is beneficial for EtOH intermediate formation and stabilization in lower energy than that for C_2H_4, and thereby promotes the pathway for EtOH.

Discussion

In summary, an assessment of a newly synthesized, silver-modified copper-oxide catalyst has confirmed that the CO_2RR to EtOH pathway is accelerated via triggering the asymmetric C–C coupling. An optimized $dCu_2O/Ag_{2.3\%}$ exhibits a FE of 40.8% and EE_{HF} of 22.3% for EtOH production in flow cell, together with boosted EtOH partial current density of 326.4 mA cm^{-2} at −0.89 V_{RHE} (with an 85 % *iR* correction). In situ ATR–IRAS spectroscopy confirmed that boosted EtOH selectivity results from moderate coordinated surface and optimal oxidation state of the

Cu sites that gives mixed $^*CO_{bridge}$ and $^*CO_{atop}$ configurations for asymmetric C–C coupling to stabilize the EtOH intermediates. This demonstrated understanding of the mechanism for electroreduction of CO_2–to– EtOH contrasts with reported, classic CO–tandem catalysis. It can be practically used to significantly boost EtOH production.

Methods

Preparation of Cu_2O, Cu_2O/Ag, and Cu_2O/Au NCs. In a typical preparation for $Cu_2O/Ag_{2.3\%}$ NCs, 0.5 mL NaOH solution (1 M) and 0.5 mL $Cu(NO_3)_2$ solution (0.1 M) were added to a 30 mL vial with 9 mL water under vigorous stirring for 5 min at RT to give a blue-color $Cu(OH)_2$ suspension. 27 mg AA was added to the vial under vigorous stirring. The suspension changed from blue color to yellow, confirming the formation of Cu_2O NCs. Following stirring for 30 min, 0.1 mL $AgNO_3$ solution (0.01 M) was added to the vial, and stirring continued for 30 min. $Cu_2O/Ag_{2.3\%}$ NCs were obtained and resulting products were collected by centrifugation and washed with EtOH. Preparation of Cu_2O and Cu_2O/Au NCs was similarly conducted, but without the addition of $AgNO_3$ and with the replacement of $AgNO_3$ with $HAuCl_4{\bullet}4H_2O$. Cu_2O/Ag and Cu_2O/Au NCs with different compositions were prepared by adding selected volumes of $AgNO_3$ and $HAuCl_4{\bullet}4H_2O$ solution (Supplementary Table 5).

Characterizations. TEM and HAADF–STEM were conducted on a FEI Tecnai F20 transmission electron microscope with an acceleration voltage 200 kV. Samples were prepared by dropping EtOH dispersions of the samples onto carbon-coated, Cu TEM grids using a pipette, and dried under ambient RT conditions. SEM images were taken with a HITACHI S–3700 cold–field emission scanning electron microscope operated at 15 kV. XRD patterns were collected on X'Pert–Pro MPD diffractometer (Netherlands PANalytical) with a Cu Kα X-ray source ($\lambda = 1.540598$ Å). XPS was determined with an SSI S–Probe XPS Spectrometer. The carbon peak at 284.6 eV was used as a reference to correct for charging effects. XAS data were collected at the TPS–44 A beamline of the National Synchrotron Radiation Research Center (NSRRC, Hsinchu, Taiwan) using a Si (111) quick-scanning monochromator, and processed according to standard procedures using the Demeter program package (Version 0.9.24).

CO_2RR test in flow cell. Electroreduction of CO_2 was tested in a microfluidics flow cell that consisted of two electrolyte chambers ($20 \times 5 \times 3$, mm) and one gas chamber ($20 \times 5 \times 5$, mm)[48]. An anion exchange membrane (Fumasep FAB–PK–130) was placed between two electrolyte chambers for products separation and ionic conduction. Catalyst-deposited GDE, micro Ag/AgCl electrode (4.0 M KCl), and Ni-foam (0.5 mm thickness), respectively, served as working electrode, reference electrode, and anode. To fabricate the working electrode, a certain amount of catalysts (3 mg) were dispersed in 1 mL EtOH with 20 μL 5 wt% Nafion solution and then sprayed onto a gas diffusion layer (CeTech, NIS1007) via airbrush. The loading amount of catalysts on GDE was controlled to ~0.44 mg cm^{-2}. The working electrode was placed between gas and catholyte chambers to ensure gaseous CO_2 diffusion and reaction at the catholyte/catalysts interface. The reference electrodes were inserted in catholyte chamber and maintained at a specified distance with the working electrode. An electrochemical workstation (CHI660, Chenhua, Shanghai) with a current amplifier was used to perform the CO_2RR test. 1 M KOH (20 mL) was circulated through the electrolyte chambers under constant flow (15 mL min^{-1}) via peristaltic pump. CO_2 was supplied into gas chambers by a mass-flow controller at a constant flow rate of 30 mL min^{-1}. Reactions were tested via chronopotentiometry at differing currents for 1 h without *iR* correction. Gas and liquid products were analyzed, respectively, via GC (Agilent 8890) and ^{1}H NMR (Agilent 600 MHz DirectDrive2 spectrometers).

Potentials were referenced to RHE and *iR* correction performed based on the following, namely:

$$E_{RHE} = E_{vs\ Ag/AgCl} + 0.059 \times pH + 0.210 + 0.85 \times iR \quad (1)$$

where i is the current at each applied potential and R the equivalent series resistance measured via electrochemical impedance spectroscopy in the frequency.

FE for the formation of CO_2RR product was computed from:

$$FE = eF \times n/Q = eF \times n/(I \times t) \quad (2)$$

in which e is the number of transferred electrons for each product, F the Faraday constant, Q charge, I applied current, t reaction time, and n total product (in mole).

EE_{HC} was computed on the basis of the cathodic CO_2RR coupled with the anodic oxygen evolution reaction ($O_2 + 4H^+ + 4e^- \leftrightarrow 2H_2O$; 1.23 V *vs* RHE) from:

$$EE_{HC} = \frac{E^{\circ}_{oe} - E^{\circ}_{red}}{E_{oe} - E_{red}} \times FE_{EtOH} \quad (3)$$

where $E_{oe}{}^{o}$ and $E_{red}{}^{o}$ are, respectively, the thermodynamic potential for oxygen evolution and CO_2RR to EtOH (0.08 V vs RHE), E_{oe} and E_{red} applied potentials at, respectively, anode and cathode. For the computation of the half-cell EE, the anodic reaction was assumed to occur with an overpotential of 0 V, that is, $E_{oe} = 1.23$ V.

CO_2RR test in MEA. Electroreduction of CO_2 in MEA consisted of two titanium backplates (TA2 grade) with a 4.0 cm^2 serpentine flow field, and MEA. Catalyst-deposited GDE (~0.44 mg cm^{-2} for $Cu_2O/Ag_{2.3\%}$ NCs) and Ni-foam (0.5 mm thickness) were used, respectively, as cathode and anode. The cathode and anode were pressed onto sides of the anion exchange membrane (Sustainion 37–50, Dioxide Materials). The gap between the electrodes was minimized to reduce ohmic loss. Gaseous CO_2 (30 mL min^{-1}) was passed behind the GDL to contact the catalyst, and 0.1 M solution was used as the anolyte which was circulated via pump at 20 mL min^{-1}. CO_2RR performance for MEA was evaluated by applying different currents with a current amplifier in the two-electrode system at the CHI660 (Chenhua, Shanghai) electrochemical workstation. Cathodic gas products were vented through a simplified cold–trap to collect permeable liquid prior to gas chromatograph testing. FE values for the liquid products were computed based on the total mass of product collected on anode and cathode.

ECSA measurement. ECSA was measured by double-layer capacitance (DLC) and Pb underpotential deposition (Pb UPD) methods. All experiments are conducted in the flow cell and the used catalysts are obtained following activation under CO_2RR. For DLC method, Cyclic Voltammetry (CV) scans were conducted at the potential range from 0.15 to 0.20 V vs RHE with increasing scan rates of 10, 20, 40, 60, 80, and 100 mV s^{-1}. The capacitance currents at 0.17 V vs RHE were plotted against the scan rates, and the double-layer capacitance (C_{dl}, mF cm^{-2}) was derived from the slope according to the following:

$$C_{dl} = I/v \quad (4)$$

where I is the capacitance current (half of the difference between the anodic current density and cathodic current density, $(J_a - J_c)/2$), and v is the scan rate.

For Pb UPD method, the CV scans were conducted in Ar-saturated 0.01 M $HClO_4$ and 1 mM $PbCl_2$ at the potential range from 0.15 to 0.20 V *vs* RHE with scan rates of 10 mV s^{-1}. The ECSA of catalysts was determined according to the following:

$$ECSA_{Pb\ UPD} = A_{Pb\ UPD}/(320\mu C cm^{-2} v) \quad (5)$$

where $A_{Pb\ UPD}$ is the peak area of monolayer Pb stripping, v the scan rate and the constant 320 μC cm^{-2} is the charge density factor for the UPD of Pb on copper[33].

In situ ATR–IRAS measurement. In situ ATR–IRAS was performed on a Nicolet iS20 spectrometer equipped with an HgCdTe (MCT) detector and a VeeMax III (PIKE Technologies) accessory. The measurement was conducted in a homemade electrochemical single-cell furnished with Pt–wire and Ag/AgCl as counter and reference electrodes. A fixed-angle Ge prism (60°) coated with catalysts embed into the bottom of the cell served as the working electrode. Before testing, the detector was cooled with liquid nitrogen for at least 30 min to maintain a stable signal. Chronoamperometry was used for CO_2RR test and was accompanied by the spectrum collection (32 scans, 4 cm^{-1} resolution). All spectra were subtracted with the background.

Data availability

Data that support findings from this study are available from the corresponding author on reasonable request.

Received: 20 December 2021; Accepted: 16 June 2022;
Published online: 29 June 2022

References

1. Arakawa, H. et al. Catalysis research of relevance to carbon management: progress, challenges, and opportunities. *Chem. Rev.* **101**, 953–996 (2001).
2. Jouny, M., Luc, W. & Jiao, F. General techno–economic analysis of CO_2 electrolysis systems. *Ind. Eng. Chem. Res.* **57**, 2165–2177 (2018).
3. Birdja, Y. Y. et al. Advances and challenges in understanding the electrocatalytic conversion of carbon dioxide to fuels. *Nat. Energy* **4**, 732–745 (2019).
4. Qiao, J., Liu, Y., Hong, F. & Zhang, J. A review of catalysts for the electroreduction of carbon dioxide to produce low–carbon fuels. *Chem. Soc. Rev.* **43**, 631–675 (2014).
5. Ross, M. B. et al. Designing materials for electrochemical carbon dioxide recycling. *Nat. Catal.* **2**, 648–658 (2019).

6. Gao, D., Arán–Ais, R. M., Jeon, H. S. & Roldan Cuenya, B. Rational catalyst and electrolyte design for CO_2 electroreduction towards multicarbon products. *Nat. Catal.* **2**, 198–210 (2019).
7. Kuhl, K. P. et al. Electrocatalytic conversion of carbon dioxide to methane and methanol on transition metal surfaces. *J. Am. Chem. Soc.* **136**, 14107–14113 (2014).
8. Verma, S. et al. Insights into the low overpotential electroreduction of CO_2 to CO on a supported gold catalyst in an alkaline flow electrolyzer. *ACS Energy Lett.* **3**, 193–198 (2018).
9. Nitopi, S. et al. Progress and perspectives of electrochemical CO_2 reduction on copper in aqueous electrolyte. *Chem. Rev.* **119**, 7610–7672 (2019).
10. Kuhl, K. P., Cave, E. R., Abram, D. N. & Jaramillo, T. F. New insights into the electrochemical reduction of carbon dioxide on metallic copper surfaces. *Energy Environ. Sci.* **5**, 7050–7059 (2012).
11. Dinh, C.–T. et al. CO_2 electroreduction to ethylene via hydroxide–mediated copper catalysis at an abrupt interface. *Science* **360**, 783–787 (2018).
12. Nguyen, T. N. et al. Electrochemical CO_2 reduction to ethanol: from mechanistic understanding to catalyst design. *J. Mater. Chem. A* **9**, 12474–12494 (2021).
13. Bushuyev, O. S. et al. What should we make with CO_2 and How can we make it? *Joule* **2**, 825–832 (2018).
14. Zheng, Y. et al. Understanding the roadmap for electrochemical reduction of CO_2 to multi–carbon oxygenates and hydrocarbons on copper–based catalysts. *J. Am. Chem. Soc.* **141**, 7646–7659 (2019).
15. Vasileff, A., Xu, C., Jiao, Y., Zheng, Y. & Qiao, S. –Z. Surface and interface engineering in copper–based bimetallic materials for selective CO_2 electroreduction. *Chem* **4**, 1809–1831 (2018).
16. Wang, P. et al. Phase and structure engineering of copper tin heterostructures for efficient electrochemical carbon dioxide reduction. *Nat. Commun.* **9**, 4933 (2018).
17. Huang, J., Mensi, M., Oveisi, E., Mantella, V. & Buonsanti, R. Structural sensitivities in bimetallic catalysts for electrochemical CO_2 reduction revealed by Ag–Cu nanodimers. *J. Am. Chem. Soc.* **141**, 2490–2499 (2019).
18. Zhuang, T.–T. et al. Steering post–C–C coupling selectivity enables high efficiency electroreduction of carbon dioxide to multi–carbon alcohols. *Nat. Catal.* **1**, 421–428 (2018).
19. Ma, W. et al. Electrocatalytic reduction of CO_2 to ethylene and ethanol through hydrogen–assisted C–C coupling over fluorine–modified copper. *Nat. Catal.* **3**, 478–487 (2020).
20. Zhou, Y. et al. Dopant–induced electron localization drives CO_2 reduction to C_2 hydrocarbons. *Nat. Chem.* **10**, 974–980 (2018).
21. Hoang, T. T. H., Ma, S., Gold, J. I., Kenis, P. J. A. & Gewirth, A. A. Nanoporous copper films by additive–controlled electrodeposition: CO_2 reduction catalysis. *ACS Catal.* **7**, 3313–3321 (2017).
22. Lee, S., Park, G. & Lee, J. Importance of Ag–Cu biphasic boundaries for selective electrochemical reduction of CO_2 to ethanol. *ACS Catal.* **7**, 8594–8604 (2017).
23. She, X. et al. Tandem electrodes for carbon dioxide reduction into C_{2+} products at simultaneously high production efficiency and rate. *Cell Rep. Phys. Sci.* **1**, 100051 (2020).
24. Morales–Guio, C. G. et al. Improved CO_2 reduction activity towards C_{2+} alcohols on a tandem gold on copper electrocatalyst. *Nat. Catal.* **1**, 764–771 (2018).
25. Lv, X. et al. Electron–deficient Cu sites on Cu_3Ag_1 catalyst promoting CO_2 electroreduction to alcohols. *Adv. Energy Mater.* **10**, 2001987 (2020).
26. Clark, E. L., Hahn, C., Jaramillo, T. F. & Bell, A. T. Electrochemical CO_2 reduction over compressively strained CuAg surface alloys with enhanced multi–carbon oxygenate selectivity. *J. Am. Chem. Soc.* **139**, 15848–15857 (2017).
27. Li, Y. C. et al. Binding site diversity promotes CO_2 electroreduction to ethanol. *J. Am. Chem. Soc.* **141**, 8584–8591 (2019).
28. Chen, C. et al. Cu–Ag tandem catalysts for high–rate CO_2 electrolysis toward multicarbons. *Joule* **4**, 1688–1699 (2020).
29. Li, F. et al. Cooperative CO_2–to–ethanol conversion via enriched intermediates at molecule–metal catalyst interfaces. *Nat. Catal.* **3**, 75–82 (2020).
30. Ren, D., Ang, B. S. H. & Yeo, B. S. Tuning the selectivity of carbon dioxide electroreduction toward ethanol on oxide–derived Cu_xZn catalysts. *ACS Catal.* **6**, 8239–8247 (2016).
31. Lv, J.–J. et al. A highly porous copper electrocatalyst for carbon dioxide reduction. *Adv. Mater.* **30**, 1803111 (2018).
32. Ma, S. et al. One–step electrosynthesis of ethylene and ethanol from CO_2 in an alkaline electrolyzer. *J. Power Sources* **301**, 219–228 (2016).
33. Wang, X. et al. Efficient electrically powered CO_2–to–ethanol via suppression of deoxygenation. *Nat. Energy* **5**, 478–486 (2020).
34. Luo, M. et al. Hydroxide promotes carbon dioxide electroreduction to ethanol on copper via tuning of adsorbed hydrogen. *Nat. Commun.* **10**, 5814 (2019).
35. Hoang, T. T. H. et al. Nanoporous copper–silver alloys by additive–controlled electrodeposition for the selective electroreduction of CO_2 to ethylene and ethanol. *J. Am. Chem. Soc.* **140**, 5791–5797 (2018).
36. Su, X. et al. Hierarchically porous Cu/Zn bimetallic catalysts for highly selective CO_2 electroreduction to liquid C_2 products. *Appl. Catal. B* **269**, 118800 (2020).
37. Kim, C. et al. Cu/Cu_2O interconnected porous aerogel catalyst for highly productive electrosynthesis of ethanol from CO_2. *Adv. Funct. Mater.* **31**, 2102142 (2021).
38. Kim, J. Y. et al. Synergistic effect of Cu_2O mesh pattern on high-facet Cu surface for selective CO_2 electroreduction to ethanol. *Adv. Mater.* **34**, 2106028 (2021).
39. Jung, H. et al. Electrochemical fragmentation of Cu_2O nanoparticles enhancing selective C–C coupling from CO_2 reduction reaction. *J. Am. Chem. Soc.* **141**, 4624–4633 (2019).
40. Lum, Y., Cheng, T., Goddard, W. A. & Ager, J. W. Electrochemical CO reduction builds solvent water into oxygenate products. *J. Am. Chem. Soc.* **140**, 9337–9340 (2018).
41. Wang, L. et al. Electrochemical carbon monoxide reduction on polycrystalline copper: effects of potential, pressure, and pH on selectivity toward multicarbon and oxygenated products. *ACS Catal.* **8**, 7445–7454 (2018).
42. Zhang, W. et al. Atypical oxygen–bearing copper boosts ethylene selectivity toward electrocatalytic CO_2 reduction. *J. Am. Chem. Soc.* **142**, 11417–11427 (2020).
43. Zhu, S., Li, T., Cai, W.–B. & Shao, M. CO_2 Electrochemical reduction as probed through infrared spectroscopy. *ACS Energy Lett.* **4**, 682–689 (2019).
44. Katayama, Y. et al. An in situ surface–enhanced infrared absorption spectroscopy study of electrochemical CO_2 reduction: selectivity dependence on surface C–bound and O/bound reaction intermediates. *J. Phys. Chem. C* **123**, 5951–5963 (2019).
45. Chou, T.–C. et al. Controlling the oxidation state of the Cu electrode and reaction intermediates for electrochemical CO_2 reduction to ethylene. *J. Am. Chem. Soc.* **142**, 2857–2867 (2020).
46. Shen, H. et al. Asymmetrical C–C coupling for electroreduction of CO on bimetallic Cu–Pd catalysts. *ACS Catal.* **12**, 5275–5283 (2022).
47. Chen, X. et al. Electrochemical CO_2–to–ethylene conversion on polyamine–incorporated Cu electrodes. *Nat. Catal.* **4**, 20–27 (2021).
48. Wang, P. et al. Synergized Cu/Pb core/shell electrocatalyst for high-efficiency CO_2 reduction to C_{2+} liquids. *ACS Nano* **15**, 1039–1047 (2021).

Acknowledgements

This work was financially supported by the Australian Research Council (ARC) through Discovery Project [FL170100154, DP220102596 (S.Z.Q.)], the National Key R&D Program of China [2020YFB1505802 (X.H.)], Ministry of Science and Technology [2017YFA0208200, 2016YFA0204100 (X.H.)], National Natural Science Foundation of China [21903058, 22173066, 22103054 (T.C.) and 22025108, 2212100020 (X.H)], Natural Science Foundation of Jiangsu Higher Education Institutions [BK20190810 (T.C.)] and Start-up support from Xiamen University (X.H.). T.C. gratefully acknowledges support from the Collaborative Innovation Center of Suzhou Nano Science & Technology, the 111 Project, Joint International Research Laboratory of Carbon-Based Functional Materials and Devices.

Author contributions

S.Z.Q. and X.H. conceived and supervised the research. X.H. and P.W. designed and conducted the experiments. P.W., H.Y., X.H., and S.Z.Q. performed data analyses. C.T., Y.W., T.C., and Y.Z. participated in experiments and characterizations. P.W., K.D., X.H., and S.Z.Q. wrote and corrected the paper. All authors discussed results and commented on the manuscript.

Competing interests

The authors declare no competing interests.

Additional information

Supplementary information The online version contains supplementary material available at https://doi.org/10.1038/s41467-022-31427-9.

Correspondence and requests for materials should be addressed to Xiaoqing Huang or Shi-Zhang Qiao.

Peer review information *Nature Communications* thanks Hee-Tae Jung and the other, anonymous, reviewer(s) for their contribution to the peer review of this work.